

# Another face of Lorenz–Mie scattering: monodisperse distributions of spheres produce Lissajous-like patterns

Alfons G. Hoekstra, Richard M. P. Doornbos, Kirsten E. I. Deurloo,  
Herke Jan Noordmans, Bart G. de Grooth, and Peter M. A. Sloot

The complete scattering matrix  $\mathbf{S}$  of spheres was measured with a flow cytometer. The experimental equipment allows simultaneous detection of two scattering-matrix elements for every sphere in the distribution. Two-parameter scatterplots with  $x$  and  $y$  coordinates determined by the  $\mathbf{S}_{11} + \mathbf{S}_{ij}$  and  $\mathbf{S}_{11} - \mathbf{S}_{ij}$  values are measured. Samples of spheres with very narrow size distributions ( $< 1\%$ ) were analyzed with a FlowCytometer, and they produced unexpected two-parameter scatterplots. Instead of compact distributions we observed Lissajous-like loops. Simulation of the scatterplots, using Lorenz–Mie theory, shows that these loops are due not to experimental errors but to true Lorenz–Mie scattering. It is shown that the loops originate from the sensitivity of the scattered field on the radius of the spheres. This paper demonstrates that the interpretation of rare events and hidden features in flow cytometry needs reconsideration.

**Key words:** Polarized-light scattering, Mueller matrix, side scattering, flow cytometry, two-parameter scatterplot.

## 1. Introduction

The problem of scattering of electromagnetic plane waves by an isotropic, homogeneous sphere of arbitrary size and refractive index was solved in 1890 by Lorenz.<sup>1</sup> Eighteen years later Mie, independent of Lorenz, arrived at the same exact analytical solution.<sup>2</sup> An excellent historical account of these important results can be found in the proceedings of the Ludvig V. Lorenz session of the Optical Particle Sizing conference of 1990.<sup>3</sup> The mathematical richness of the formula is amazing and has inspired many researchers to probe in still more detail the (differential) cross sections as a function of the radius or the refractive index of the sphere or as a function of the wavelength of the incident light. The advent of

modern computers and the development of efficient algorithms to calculate the complex functions appearing in the Lorenz–Mie scattering formula stimulated these efforts even more.

The Lorenz–Mie scattering formula possesses some remarkable properties, most of which were demonstrated in scattering experiments. Well-known examples are the interference and ripple structure of the extinction cross section (e.g., Ref. 4), glare points (e.g., Ref. 5), and rainbows and glories (e.g., Refs. 6 and 7). Despite the fact that the Lorenz–Mie solution has been known for more than a century, active research on the wealth of physically intriguing phenomena contained in Lorenz–Mie scattering continues. For instance, the internal electric field in the sphere is receiving more and more attention (e.g., Ref. 8).

Lorenz–Mie scattering comes in many disguises. Thurn and Kiefer measured Raman spectra from optically levitated glass and liquid spheres and observed a ripple structure superimposed on the bulk Raman spectrum.<sup>9</sup> The ripples proved to be the result of structural resonances of the internal electric field, as could be demonstrated with the Lorenz–Mie theory. These structural-resonance features could also be detected in stimulated Raman scattering from individual liquid droplets.<sup>10</sup> Tzeng *et al.* observed

A. G. Hoekstra and P. M. A. Sloot are with the Parallel Scientific Computing Group, Department of Computer Systems, Faculty of Mathematics and Computer Science, University of Amsterdam, Kruislaan 403, 1098 SJ Amsterdam, The Netherlands. R. M. P. Doornbos, K. E. I. Deurloo, H. J. Noordmans, and B. G. de Grooth are with the Cell Characterization Group, Department of Technical Optics, Faculty of Applied Physics, University of Twente, P.O. Box 217, 7500 AE Enschede, The Netherlands.

Received 10 November 1992; revised manuscript received 12 July 1993.

0003-6935/94/030494-07\$06.00/0.

© 1994 Optical Society of America.

laser emission from small droplets at Lorenz-Mie resonance wavelengths.<sup>11</sup> These three effects are all due to the enhancement of the internal field intensity at a structural resonance.

This paper reports on yet another face of Lorenz-Mie scattering, which is based on the extreme sensitivity of the scattered field on the radius of the sphere. We measure the total scattering matrix of spheres with a narrow size distribution ( $\Delta r/r \sim 1\%$ , where  $r$  is the radius of the sphere) in a dedicated flow cytometer (FCM). This experimental equipment allows us to measure  $S_{11} + S_{ij}$  and  $S_{11} - S_{ij}$  ( $ij = 12, 33, 34$  and  $S$  is the  $4 \times 4$  scattering matrix) simultaneously for every single sphere in the distribution. Flow cytometry data are usually analyzed by generating an  $N$ -dimensional histogram ( $N$  being the number of observables per particle, here  $N = 2$ ) from the experimental data and trying to identify different data clusters in the histogram with different particles in the sample.<sup>12</sup> At first sight a distribution of homogeneous spheres with a very narrow Gaussian size distribution is expected to produce a single, narrow, Gaussian-like two-dimensional histogram. However, it turned out that the measured histograms are all but Gaussian.

Here we explain that this effect is not an experimental error but is due to true Lorenz-Mie scattering. We calculate the two-dimensional histograms and obtain agreement between theory and experiment. In Section 2 the theoretical and experimental background is briefly addressed, and the results are presented in Section 3 and discussed in Section 4. Emphasis is placed on the agreement between theory and experiment, but the consequences of this paper for routine FCM experiments are also briefly pointed out. In Section 5 conclusions are drawn.

## 2. Materials and Methods

### A. Flow Cytometry

Flow cytometry<sup>12</sup> is an important technique in the biological sciences to identify and separate various populations of, for instance, white bloodcells. Hydrodynamic focusing forces the cells to flow through a focused laser beam one by one. Usually the cells are stained with fluorescent probes, and the fluorescence of a cell in the laser beam is measured. Furthermore, the forward- and sideward-scattered light are used as important additional parameters for the analysis. In this way we can measure several fluorescence and elastic light scattering signals for each cell in the sample.

Sloot *et al.* argue that in many research and clinical applications staining of cells is undesirable.<sup>13</sup> As a consequence a complete characterization of the sample must be obtained solely on the basis of elastic light scattering measurements. We suspect that this characterization is possible only from measurement of suitable combinations of scattering-matrix elements in the three principal FCM directions (forward-, sideward-, and backward-scattered light).<sup>13</sup> The depolarization experiments in which de Grooth *et al.*<sup>14</sup>

distinguish between neutrophilic and eosinophilic granulocytes are a good illustration of this point.

We developed optics to measure the total scattering matrix in a FCM and showed that quantitative determination of the scattering-matrix elements of particles in flow is possible.<sup>13,15</sup> The measuring principle was straightforward: a polarizer  $P$  was situated in the incident beam, and an analyzer  $A$  was situated just before a detector in one of the principal directions. The matrix elements are obtained by measuring scattered intensities for various  $P$ - $A$  combinations. We have extended the optics to allow simultaneous measurement of two  $P$ - $A$  combinations in the side-scattering direction; see Fig. 1.

A laser beam ( $\lambda = 0.6328 \mu\text{m}$ ) is focused by the circular lens,  $l1$ , on the cells flowing through the cuvet and polarized by the polarizer,  $P$ . The beam-waist radius in the focal point is  $12.5 \mu\text{m}$ . After  $P$  the incident beam is either linearly or circularly polarized. The forward-scattered light is detected by a silicon detector  $d1$ . Lens  $l2$ , a microscope objective ( $20\times$ , N.A. = 0.4), collects the scattered light for  $72.5^\circ < \theta < 107.5^\circ$ , where  $\theta$  is the usual scattering angle. The sideward-scattered light is divided in two beams by a beam splitter  $B$ . The beams are directed onto different analyzers ( $A1$  and  $A2$ ), and the intensity after the analyzers is measured by the photomultipliers,  $d2$  and  $d3$ . The measuring principle is the same as described by Sloot *et al.*,<sup>13</sup> however, here it is possible to measure a  $P$ - $A1$  and  $P$ - $A2$  combination for every single cell. This allows a direct measurement of single elements of the scattering matrix. Details of this equipment and its application to measurement of the scattering matrix of white bloodcells will be published elsewhere.

### B. Data Handling

Our equipment measures three parameters for each cell: the forward-scattered light and two  $P$ - $A$  intensities in the sideward direction. The analog signals

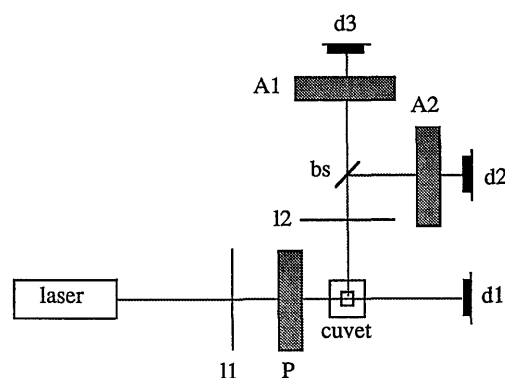


Fig. 1. Schematic drawing of the optical system of the FlowCytometer. The laser beam is focused by lens  $l1$  on a cell flowing through the cuvet. The incident beam is polarized by means of the polarizer,  $P$ . The intensity of the forward-scattered light is measured by detector  $d1$ , and the sideward-scattered light is focused by lens  $l2$  on detectors  $d2$  and  $d3$ . The side-scattering signals are passed through two different analyzers,  $A1$  and  $A2$ .  $B$ , beam splitter.

are digitized by 12-bit analog-to-digital converters and stored in the memory of the controlling computer. In every run 4096 particles are measured, and the results are stored on hard disk for off-line analysis.

The data are plotted in two-parameter scatterplots in which each cell is represented by a dot in an  $x$ - $y$  plot. The  $x$  and  $y$  coordinates are determined by one of the three measured parameters. Figure 2 gives an example of a scatterplot for polystyrene spheres with a mean diameter of 1.98  $\mu\text{m}$ . The forward scattering is drawn along the  $x$ -axis and one side-scattering signal is drawn along the  $y$ -axis. The spheres appear as a cloud of points in the scatterplot.

The shape of the data cloud in the scatterplots and the physical interpretation are the main items of this paper.

### C. Polystyrene Spheres

The experiments were performed with polystyrene microspheres (model 1135D) from Duke Scientific (San Antonio Palo Alto, Calif.). The diameters of the spheres are  $1.98 \pm 0.05$  and  $7.04 \pm 0.05$   $\mu\text{m}$ .

In addition to the diameter of the sphere, Lorenz-Mie calculations require the relative refractive index of the sphere. The refractive index of distilled water, in which the spheres are suspended, and polystyrene can be calculated with<sup>16</sup>

$$n_{\text{water}} = n_0 + n_2/\lambda^2 + n_4/\lambda^4. \quad (1)$$

where  $\lambda$  is in micrometers and  $n_0 = 1.3236$ ,  $n_2 = 3.35 \times 10^{-3}$ , and  $n_4 = -3.45 \times 10^{-5}$  for water and  $n_0 = 1.5711$ ,  $n_2 = 4.82 \times 10^{-3}$ , and  $n_4 = 6.78 \times 10^{-4}$  for polystyrene. In our case  $\lambda = 0.6328$   $\mu\text{m}$ , which gives us  $n_{\text{water}} = 1.3318$  and  $n_{\text{polysty}} = 1.5874$ . In the

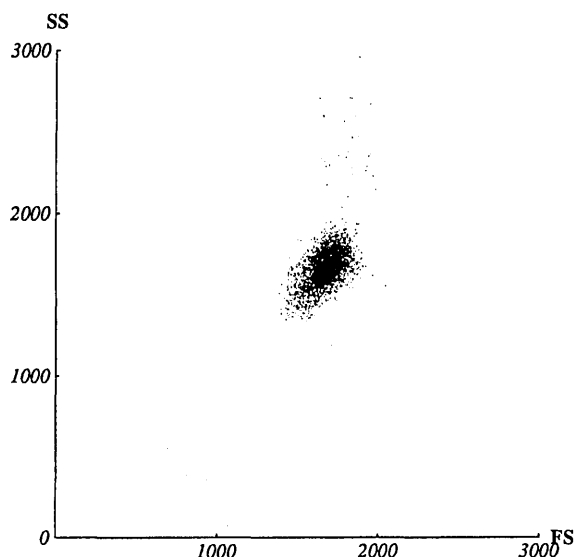


Fig. 2. Example of a two-parameter scatterplot for a large number of polystyrene spheres with a mean diameter of 1.98  $\mu\text{m}$ , measured with a FlowCytometer. The wavelength was 0.6328  $\mu\text{m}$ . Every dot represents a single sphere; the value of the  $x$  coordinate is the intensity of the forward-scattered (FS) light, and the value of the  $y$ -coordinate is the intensity of the sideward-scattered (SS) light. The intensities are in arbitrary units.

calculations we use

$$n_{\text{rel}} = n_{\text{polysty}}/n_{\text{water}} = 1.192,$$

and diameters as reported above.

### D. Simulation of the Scatterplots

To simulate the two-parameter scatterplots the intensities measured by the sideward detectors must be calculated. For spheres, when the P-A combinations are used as described by Sloot *et al.*, the intensity of the scattered light after analyzers A1 and A2 is<sup>13</sup>

$$I_A = I_0 C(\mathbf{S}_{11} \pm \mathbf{S}_{ij}), \quad ij = 12, 33, 34, \quad (2)$$

where  $I_0$  is the intensity of the laser beam,  $C$  is an apparatus constant, and  $\mathbf{S}$  is the  $4 \times 4$  scattering matrix of the sphere. The total intensity on the detector is obtained by integrating over the full solid angle,  $d\Omega$ , defined by the field of view of the objective,

$$\begin{aligned} I_{\text{det}} &= \int_{d\Omega} I_A d\omega = I_0 C \left( \int_{d\Omega} \mathbf{S}_{11} d\omega \pm \int_{d\Omega} \mathbf{S}_{ij} d\omega \right) \\ &= I_0 C(\mathbf{s}_{11} \pm \mathbf{s}_{ij}), \end{aligned} \quad (3)$$

where  $\mathbf{s}_{ij}$  is an integrated matrix element.

To calculate the scattering matrix of a sphere in a focused laser beam, we cannot apply the traditional Lorenz-Mie theory. Here we must rely on the generalized Lorenz-Mie theory, which describes the scattering of a sphere in a Gaussian beam.<sup>17</sup> The  $\mathbf{g}_n$  coefficients appearing in this theory are calculated with the localized interpretation.<sup>18,19</sup> We use the same programs as described in Ref. 13. The beam-waist radius of the Gaussian beam is 12.5  $\mu\text{m}$  (see Section 2.A.). The particles are located in the focal point of the beam.

The procedure to generate a simulated scatterplot is as follows. First we calculate the scattering matrix  $\mathbf{S}(\theta)$  as a function of the scattering angle  $\theta$  (resolution  $d\theta = 0.1^\circ$ ) for a sphere with relative refractive index 1.192, diameter  $d$ , wavelength of the incident light 0.6328  $\mu\text{m}$ , and the appropriate beam-waist diameter. Then the integrated scattering elements  $\mathbf{s}_{ij}$  are calculated, as described in Ref. 13. The  $\mathbf{s}_{ij}$  are calculated for 500 different values of  $d$  in the range

$$d_{\text{mean}} - 4\sigma_d \leq d \leq d_{\text{mean}} + 4\sigma_d, \quad (4)$$

where  $d_{\text{mean}}$  is the mean diameter in the distribution and  $\sigma_d$  is the standard deviation (assuming a normal distribution in diameter). This results in arrays of  $\mathbf{s}_{ij}(d_i)$ , with discrete values  $d_i$  as defined above. For every  $d_i$  the  $\mathbf{s}_{ij}(d_i)$  determine coordinates of a dot in the two-parameter scatterplot, and the total scatterplot is generated by drawing dots for every value of  $d_i$ . To simulate the relative occurrence of spheres with diameter  $d_i$  in the distribution, we weight the radius of the dots in the scatterplot with a Gaussian func-

tion:

$$r_{\text{dot}} = r_{\text{max}} \exp \left[ -\frac{(d_i - d_m)^2}{2\sigma_d^2} \right], \quad (5)$$

where  $r_{\text{dot}}$  is the radius of the dot for a sphere with diameter  $d_i$ , and  $r_{\text{max}}$  is the maximum radius of dots in the simulated scatterplots.

#### E. Comparison Between Theory and Experiment

The result of the calculations is a set  $(\mathbf{s}_{11}, \mathbf{s}_{12}, \mathbf{s}_{33}, \mathbf{s}_{34})_i$ , where  $i$  covers all the values of  $d$ . The measurements give arrays of detector signals, as in Eq. (3). We need an independent scaling for both theory and experiment to compare the two. The experimental results are scaled such that the apparatus constants,  $I_0$  and  $C$ , are removed and the experimental scatterplots are entirely described in terms of scattering-matrix elements. The scaling factor for the experimental results is

$$\text{scale}_{\text{ex}} = \frac{1}{2p} \sum_{i=1}^p (I_{A1}^i + I_{A2}^i) = \frac{1}{p} I_0 C \sum_{i=1}^p \mathbf{s}_{11}^i, \quad (6)$$

with  $p$  the total number of measured spheres and  $I_{A1}$  and  $I_{A2}$  the intensities of the scattered light after analyzers A1 and A2. Dividing the measurements by this factor results in two parameters for each measured sphere, independent of  $I_0$  and  $C$ :

$$\left( \frac{1}{p} \sum_{i=1}^p \mathbf{s}_{11}^i \right)^{-1} (\mathbf{s}_{11} \pm \mathbf{s}_{ij}). \quad (7)$$

These normalized experimental parameters are used as  $(x, y)$  coordinates in the scatterplots.

The term

$$\frac{1}{p} \sum_{i=1}^p \mathbf{s}_{11}^i$$

is the weighted mean,  $\mathbf{s}_{11}$  of the distribution of spheres. If we assume a normal distribution in diameter, this term is easily calculated from theory:

$$\overline{\mathbf{s}_{11}} = \int_0^\infty \frac{1}{\sigma_d \sqrt{2\pi}} \exp \left[ -\frac{(d - d_{\text{mean}})^2}{2\sigma_d^2} \right] \mathbf{s}_{11}(d) \delta d. \quad (8)$$

This integral is approximated by numerical evaluation for  $d_{\text{mean}} - 4\sigma_d \leq d \leq d_{\text{mean}} + 4\sigma_d$ , using Simpson's rule. The integrated scattering matrix elements calculated above are divided by the value of this integral. After scaling is done, we may compare theory and experiment. In the sequel to this paper the scatterplots of experimental and theoretical data are always scaled accordingly.

### 3. Results

This section presents the results of measurements and calculations of two-parameter scatterplots of spheres. The normalized experimental and theoretical

cal results are shown in one figure. The  $x$ -axis always gives the  $\mathbf{s}_{11} + \mathbf{s}_{ij}$  signal, and the  $y$ -axis always gives the  $\mathbf{s}_{11} - \mathbf{s}_{ij}$  signal, with  $ij$  as before. The dots in the theoretical curves are placed according to Eq. (5). The insets in Figs. 3–5, below, show the theoretical curves without scaling of the dot diameters.

Figure 3 shows the  $(\mathbf{s}_{11} + \mathbf{s}_{12}, \mathbf{s}_{11} - \mathbf{s}_{12})$  scatterplot for the 7.04- $\mu\text{m}$  spheres; the  $(\mathbf{s}_{11} + \mathbf{s}_{33}, \mathbf{s}_{11} - \mathbf{s}_{33})$  and  $(\mathbf{s}_{11} + \mathbf{s}_{34}, \mathbf{s}_{11} - \mathbf{s}_{34})$  scatterplots for this sample are shown in Figs. 4 and 5, respectively. Finally, the  $(\mathbf{s}_{11} + \mathbf{s}_{12}, \mathbf{s}_{11} - \mathbf{s}_{12})$  scatterplot for the 1.98- $\mu\text{m}$  spheres is shown in Fig. 6.

### 4. Discussion

Figures 3, 4, and 5 show the three normalized experimental and theoretical scatterplots for the 7.04- $\mu\text{m}$  spheres. All three experimental scatterplots are loops; this is most obvious for the  $(\mathbf{s}_{11} + \mathbf{s}_{12}, \mathbf{s}_{11} - \mathbf{s}_{12})$  and the  $(\mathbf{s}_{11} + \mathbf{s}_{34}, \mathbf{s}_{11} - \mathbf{s}_{34})$  scatterplot.

The occurrence of loops in the scatterplots depends on the diameter of the spheres. Figure 6 is the  $(\mathbf{s}_{11} + \mathbf{s}_{12}, \mathbf{s}_{11} - \mathbf{s}_{12})$  scatterplot for the 1.98- $\mu\text{m}$  sphere. The experimental scatterplot is a dense distribution of points, in agreement with the theoretical results. The same holds for the other two scatterplots (data not shown).

The form and position of the normalized theoretical scatterplots for the 7.04- $\mu\text{m}$  spheres compare very well with the experimental results. The agreement between theory and experiment for the  $(\mathbf{s}_{11} + \mathbf{s}_{12}, \mathbf{s}_{11} - \mathbf{s}_{12})$  scatterplot is very good. The other two scatterplots only show a quantitative agreement between the theoretical and experimental results. Nevertheless this demonstrates that the observed

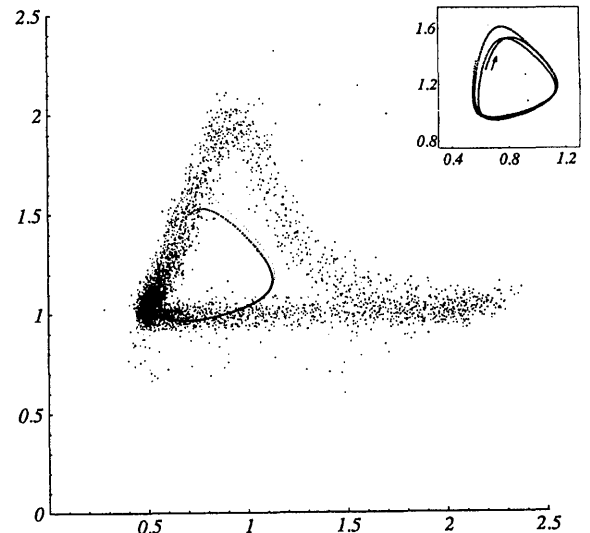


Fig. 3. Normalized experimental and theoretical  $(\mathbf{s}_{11} + \mathbf{s}_{12}, \mathbf{s}_{11} - \mathbf{s}_{12})$  scatterplot for polystyrene spheres with a mean diameter of 7.04  $\mu\text{m}$ . The horizontal axis is the  $\mathbf{s}_{11} + \mathbf{s}_{12}$  signal in the sideward direction, and the vertical axis is the  $\mathbf{s}_{11} - \mathbf{s}_{12}$  signal in the sideward direction. The inset shows the theoretical curve only, without scaling of the dot diameter. The arrow represents the starting point ( $d_i = d_{\text{mean}} - 4\sigma_d$ ) and the loop direction, as  $d_i$  increases, of the theoretical curve.

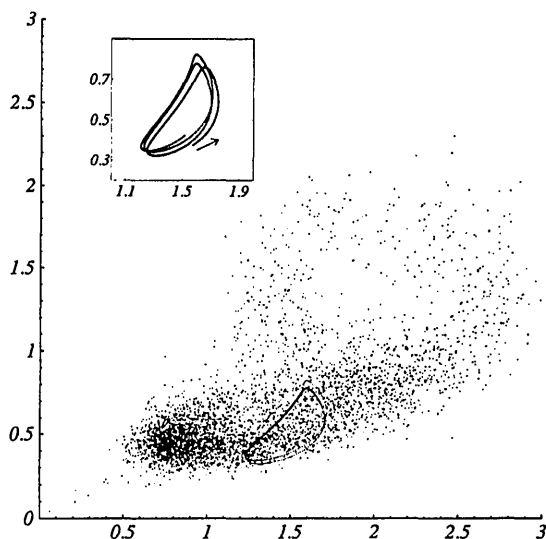


Fig. 4. Same as in Fig. 3 but for the  $(s_{11} + s_{33}, s_{11} - s_{33})$  scatterplot.

loops in the experimental plots are due to Lorenz-Mie scattering and cannot be attributed to optical misalignments or other experimental errors.

Failure to find a quantitative agreement between theory and experiment for the  $(s_{11} + s_{34}, s_{11} - s_{34})$  scatterplot is probably due to the quality of the circular analyzers that are used to measure the  $s_{34}$  terms. Without going into details here, imperfect circular analyzers will cause a mixing of the  $s_{33}$  and  $s_{34}$  terms. This effect is still under investigation.

Theory and experiment can be compared in terms of still another aspect. In the theory a normal distribution of spherical diameters was assumed, and this was simulated by weighting the radius of the dots in the scatterplot with a Gaussian function [see Eq. (5)]. The theoretical curves nicely show the distribution of the spherical diameter. However, as is obvi-

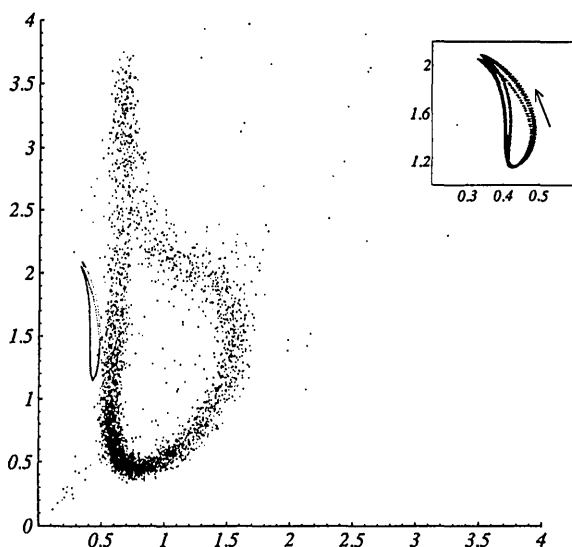


Fig. 5. Same as in Fig. 3 but for the  $(s_{11} + s_{34}, s_{11} - s_{34})$  scatterplot.

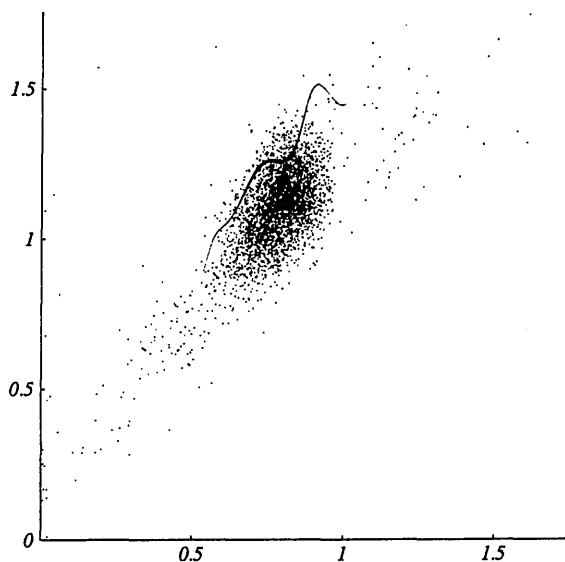


Fig. 6. Normalized experimental and theoretical  $(s_{11} + s_{12}, s_{11} - s_{12})$  scatterplot for polystyrene spheres with a mean diameter of  $1.98 \mu\text{m}$ . The horizontal axis is the  $s_{11} + s_{12}$  signal in the sideward direction, and the vertical axis is the  $s_{11} - s_{12}$  signal in the sideward direction.

ous from the scatterplots for the  $7.04\text{-}\mu\text{m}$  sphere, this distribution is in error compared with the experimental results. The experimental scatterplots have most points in the lower left of the loops, whereas the theoretical results show that most points should be distributed along a long portion of the loops. A closer look at the theoretical curves shows that this error between theory and experiment can be explained by assuming that the actual mean diameter of the spheres is somewhat larger than  $7.04 \mu\text{m}$ , the value provided by the supplier of the spheres. The insets in Figs. 3–5 show the theoretical curves, without scaling of the dot radius, and the starting points and loop directions of the curves. The starting point is for  $d = d_{\text{mean}} - 4\sigma_d$ , and for increasing diameter the curve loops in the direction of the arrow. The  $(s_{11} + s_{12}, s_{11} - s_{12})$  scatterplot loops in the clockwise direction, whereas the other two curves loop in the counterclockwise direction. If the mean diameter of the sphere is increased, the position of the dots with large diameter in the theoretical curves shifts in the loop direction. Therefore, if the mean diameter of the sphere is increased to  $7.08 \mu\text{m}$ , all three theoretical scatterplots reproduce the measured distribution correctly. Furthermore, we measured the scatterplots for a slightly larger wavelength of the incident light ( $\lambda = 0.647 \mu\text{m}$ ). In that case one expects that the same experimental loops occur but with a small shift of the distribution of the data points in the loop. In all three scatterplots we observed this shift of the data points. The direction and magnitude of the shift are in agreement with calculated values (data not shown).

The origin of the loops in the scatterplots can be understood by examining the integrated matrix elements as a function of the diameter of the sphere.

Figure 7 plots  $s_{11}$ ,  $s_{12}$ ,  $s_{33}$ , and  $s_{34}$  as a function of the diameter of the sphere for  $d$  as in Eq. (4), and  $d_{\text{mean}}$  is  $7.04 \mu\text{m}$ . The matrix elements possess an extreme sensitivity on the diameter of the sphere. For  $6.84 \mu\text{m} < d < 7.24 \mu\text{m}$ ,  $s_{11}$  goes through three minima and maxima. The amplitude of the oscillations is approximately 20% of the mean value of  $s_{11}$ . The other integrated-scattering-matrix elements have the same properties, although the oscillations are not in phase with the  $s_{11}$  oscillations. However, for spheres with  $1.78 \mu\text{m} < d < 2.18 \mu\text{m}$  the  $s_{ij}$  elements increase monotonically with increasing  $d$  (data not shown).

In the diameter range of Fig. 7 the integrated-scattering functions are almost periodic. The  $s_{11}$  strongly resembles a sine function. The other (quasi-) periodic scattering-matrix elements can be viewed as a Fourier series of sine and cosine functions. Fourier transformation of the data in Fig. 7 supports this view. For all four scattering-matrix elements the absolute value of the Fourier-transform peaks around the same ground frequency  $\nu_0$  and around higher harmonics  $k\nu_0$  (where  $k$  is an integer  $> 1$ ). The amplitude of the third and higher harmonics are negligible compared with the amplitude of the ground frequency (data not shown).

When constructing the theoretical scatterplot, we actually draw a parametric plot, with the diameter of the sphere,  $d$ , as the only parameter. The functions on the  $x$ - and  $y$ -axes of the scatterplot are approximate combinations of sines and cosines of some ground frequency and higher harmonics. Therefore the scatterplots can be viewed as Lissajous plots. The oscillations in the integrated matrix elements, which are not in phase with each other, give rise to the Lissajous loops in the two-parameter scatterplots. Note that in principle it is possible to measure more complicated scatterplots with, for example, double loops (a ground-frequency oscillation in one direction and a first-harmonic oscillation in the other direction). Actually, in one instance we measured scatterplots with such double loops. We are still working on the interpretation of these experiments.

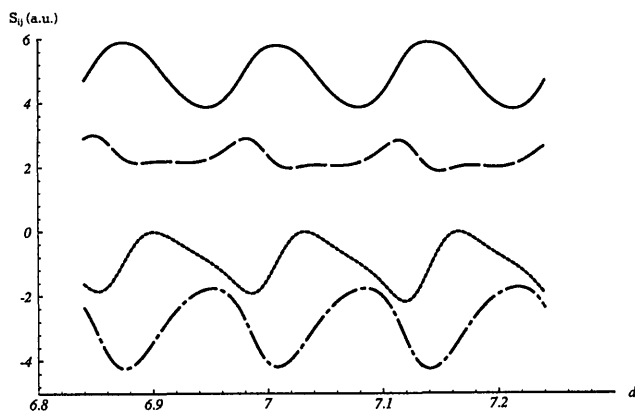


Fig. 7. Integrated-scattering-matrix elements, as a function of the diameter,  $d$ , of the sphere (in micrometers). The solid curve is  $s_{11}$ , the dotted curve is  $s_{12}$ , the dashed curve is  $s_{33}$ , and the dashed-dotted curve is  $s_{34}$ . a.u., arbitrary units.

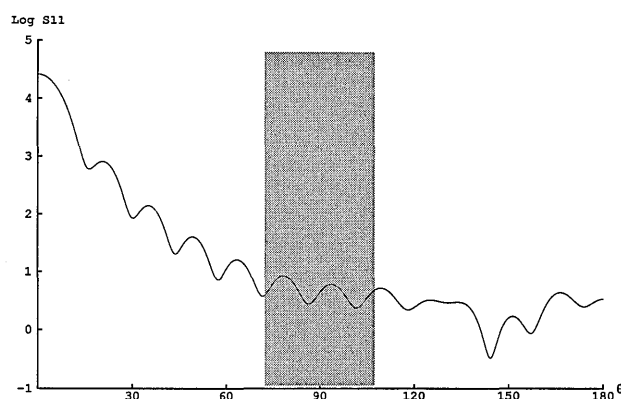


Fig. 8.  $S_{11}$  element as a function of the scattering angle  $\theta$  for  $d = 1.98 \mu\text{m}$ . The shaded area denotes the field of view of the side-scattering detectors.

Figures 8 and 9 show  $S_{11}$  as a function of the scattering angle  $\theta$  for  $d = 1.98 \mu\text{m}$  and  $7.04 \mu\text{m}$ , respectively. The shaded areas in these figures denote the field of view of the side-scattering detectors. If the diameter of the sphere is increased, the minima and maxima in  $S_{11}(\theta)$  gradually shift to the forward directions, and new minima and maxima seem to originate from  $\theta = 180^\circ$ .<sup>4</sup> Slightly increasing the size of the  $7.04\text{-}\mu\text{m}$  sphere results in entrance and exit of local minima and maxima in the field of view of the detectors, and changes in the amplitude of the minima and maxima, giving rise to the oscillations in the curves of the integrated matrix elements as a function of the diameter of the sphere (Fig. 7). The distance between the local minima and maxima in the  $S_{11}(\theta)$  curve for the  $1.98\text{-}\mu\text{m}$  sphere is too large to induce strong oscillations in the integrated matrix elements after small changes of the diameter of the sphere.

Measurement of polarized-light scattering in FCM is by no means a routine procedure yet; nevertheless our results contain an importance warning. It is common practice in FCM to measure a side-scattering signal. Because the incident light is always linearly

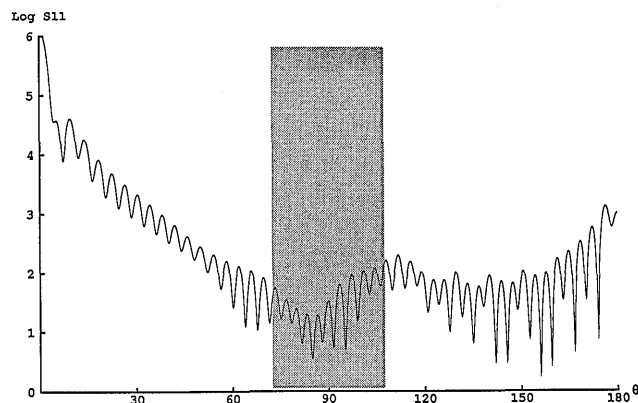


Fig. 9.  $S_{11}$  element as a function of the scattering angle  $\theta$  for  $d = 7.04 \mu\text{m}$ . The shaded bar denotes the field of view of the side-scattering detectors.

polarized (most lasers emit light that is linearly polarized, perpendicular to the scattering plane), the intensity on the side-scattering detectors is always a combination of  $s_{11}$  and  $s_{12}$ . Therefore a narrow monodisperse distribution of spheres can produce bimodal histograms in the side-scattering channels (this can be seen in Fig. 3 for the  $s_{11} + s_{12}$  signal). Especially if spheres are applied to calibrate the instrument, extra care should be taken, and small spheres should be used to avoid the above-mentioned problems. Furthermore, interpretation of rare events and hidden distributions in scatterplots requires careful analysis in view of the above-mentioned effect. We are currently investigating the extent to which the Lissajous loops can be expected in scatterplots from biological particles.

## 5. Conclusions

This paper shows yet another face of Lorenz-Mie scattering: unexpected, Lissajous-like loops in two-parameter scatterplots of spheres, as obtained by flow cytometry. The complete scattering matrix of spheres, with a very narrow distribution in size, was measured with a dedicated FlowCytometer (FCM). The measured two-parameter scatterplots can contain unexpected, Lissajous-like loops. By simulating these scatterplots, it was shown that the experimental results are true Lorenz-Mie scattering phenomena and are not due to experimental errors. The occurrence of loops in the scatterplots is dependent on the diameter of the spheres. It was shown that oscillations in the integrated matrix elements, as a function of the diameter of the sphere, form the basis for the Lissajous loops. These oscillations in turn originate from the interference structure in the differential-scattering cross sections.

A consequence of this behavior is the origin of bimodal histograms in the side-scattering channels, which are due to monodisperse samples. This will hamper the interpretation of rare events and hidden distributions in the scatterplots.

We gratefully acknowledge financial support from the Netherlands Organization for Scientific Research by matched funding from Fundamenteel Onderzoek der Materie, Stichting Informatika Onderzoek Nederland, and Foundation for Biophysics grant NWO 810-410-04 1.

## References

1. L. V. Lorenz, "Upon the light reflected and refracted by a transparent sphere," *Vidensk. Sel'sk. Shrifter* **6**, 1-62 (1890).
2. G. Mie, "Considerations on the optics of turbid media, especially colloidal metal sols," *Ann. Phys.* **25**, 377-442 (1908).
3. E. D. Hirleman, ed., *Proceedings of the Second International Congress on Optical Particle Sizing* (Arizona State University, Tempe, Ariz., 1990), p. 1; *Appl. Opt.* **30**, 688-699 (1991).
4. C. F. Bohren and D. R. Huffman, *Absorption and Scattering of Light by Small Particles* (Wiley, New York, 1983).
5. H. C. van de Hulst and R. T. Wang, "Glare point," *Appl. Opt.* **30**, 4755-6763 (1991).
6. R. T. Wang and H. C. van de Hulst, "Rainbows: Mie computations and the Airy approximation," *Appl. Opt.* **30**, 106-117 (1991).
7. H. M. Nussenzveig, "Complex angular momentum theory of the rainbow and the glory," *J. Opt. Soc. Am.* **69**, 1068-1079 (1979).
8. J. A. Lock, "Interference enhancement of the internal fields at structural scattering resonances of a coated sphere," *Appl. Opt.* **29**, 3180-3187 (1990).
9. R. Thurn and W. Kiefer, "Structural resonances observed in the Raman spectra of optically levitated liquid droplets," *Appl. Opt.* **24**, 1515-1519 (1985).
10. J. B. Show, S. X. Qian, and R. K. Chang, "Stimulated Raman scattering from individual water and ethanol droplets at morphology-dependent resonances," *Opt. Lett.* **10**, 37-39 (1985).
11. H. M. Tzeng, K. F. Wall, M. B. Long, and R. K. Chang, "Laser emission from individual droplets at wavelengths corresponding to morphology-dependent resonances," *Opt. Lett.* **9**, 499-501 (1984).
12. M. A. van Dilla, P. N. Dean, O. D. Laerum, and M. R. Melamed, *Flow Cytometry: Instrumentation and Data Analysis* (Academic, San Diego, Calif., 1985), Chap. 1.
13. P. M. A. Slood, A. G. Hoekstra, H. van der Liet, and C. G. Figdor, "Scattering matrix elements of biological particles measured in a flow through system: theory and practice," *Appl. Opt.* **28**, 1752-1762 (1989).
14. B. G. Grooth, L. W. M. M. Terstappen, G. J. Puppels, and J. Greve, "Light-scattering polarization measurements as a new parameter in flow cytometry," *Cytometry* **8**, 539-544 (1987).
15. P. M. A. Slood and A. G. Hoekstra, "Arbitrarily-shaped particles measured in flow through systems," in *Proceedings of the Second International Congress on Optical Particle Sizing*, E. D. Hirleman, ed. (Arizona State University, Tempe, Ariz., 1990), p. 605.
16. E. Gulari, "Latex particle size distributions from multiwavelength turbidity spectra," *Part. Characteriz.* **4**, 96-101 (1987).
17. G. Gouesbet, B. Maheu, and G. Gréhan, "Light scattering from a sphere arbitrarily located in a Gaussian beam, using a Bromwich formulation," *J. Opt. Soc. Am. A* **5**, 1427-1443 (1988).
18. G. Gréhan, B. Maheu, and G. Gouesbet, "Scattering of laser beams by Mie scatter centers: numerical results using a localized approximation," *Appl. Opt.* **25**, 3539-3548 (1986).
19. G. Gouesbet, G. Gréhan, and B. Maheu, "Localized interpretation to compute all the coefficients  $g_n^m$  in the generalized Lorenz-Mie theory," *J. Opt. Soc. Am. A* **7**, 998-1007 (1990).